

# Inferring Thunderstorm Occurrence from Vertical Profiles of Convection-Permitting Simulations: Physical Insights from a Physical Deep Learning Model

KIANUSCH VAHID YOUSEFNIA,<sup>a</sup> TOBIAS BÖLLE,<sup>a</sup> CHRISTOPH METZL,<sup>a</sup>

<sup>a</sup> *Deutsches Zentrum für Luft- und Raumfahrt, Institut für Physik der Atmosphäre, Oberpfaffenhofen, Germany*

**ABSTRACT:** Thunderstorms have significant social and economic impacts due to heavy precipitation, hail, lightning, and strong winds, necessitating reliable forecasts. Thunderstorm forecasts based on numerical weather prediction (NWP) often rely on single-level surrogate predictors, like convective available potential energy and precipitation rate, derived from vertical profiles of three-dimensional atmospheric variables. In this study, we develop SALAMA 1D, a deep neural network that directly infers the probability of thunderstorm occurrence from vertical profiles of ten atmospheric variables, bypassing single-level predictors. By training the model on convection-permitting NWP forecasts, we allow SALAMA 1D to flexibly identify convective patterns, with the goal of enhancing forecast accuracy. The model’s architecture is physically motivated: sparse connections encourage interactions at similar height levels, while a shuffling mechanism prevents the model from learning non-physical patterns tied to the vertical grid. SALAMA 1D is trained over Central Europe with lightning observations as the ground truth. Comparative analysis against a baseline machine learning model that uses single-level predictors shows SALAMA 1D’s superior skill across various metrics and lead times of up to at least 11 hours. Moreover, increasing the number of forecasts used to compile the training set improves skill, even when training set size is kept constant. Sensitivity analysis using saliency maps indicates that the model reconstructs environmental lapse rates and rediscovers patterns consistent with established theoretical understandings, such as positive buoyancy, convective inhibition, and ice particle formation near the tropopause, while ruling out thunderstorm occurrence based on the absence of mid-level graupel and cloud cover.

**SIGNIFICANCE STATEMENT:** This work aims to improve thunderstorm forecasting by applying machine learning to vertical atmospheric profiles from numerical weather prediction. We developed a model that incorporates physical considerations, resulting in more accurate yet computationally efficient predictions compared to conventional methods. Additionally, the model provides insights into how it identifies thunderstorm occurrence, fostering interpretability and trust. Our research demonstrates how to enhance the reliability of machine learning systems in severe weather forecasting, which is crucial for supporting timely, informed decision-making in situations that impact public safety and the economy.

## 1. Introduction

Thunderstorms can have devastating impacts on society and the economy due to accompanying phenomena such as lightning, intense precipitation (including graupel and hail), and strong winds. Severe thunderstorms may lead to flash floods, which can result in significant damage and endanger lives (Ntelekos et al. 2007; Piper et al. 2016). Additionally, thunderstorms cause harm to crops and livestock, resulting in considerable economic losses (Holle 2014). Moreover, thunderstorm occurrence affects aviation and logistics, causing costly delays and heightened safety risks (Gerz et al. 2012; Borsky and Unterberger

2019). Since climate change is expected to increase the frequency of thunderstorms (Diffenbaugh et al. 2013; Rädler et al. 2019; Taszarek et al. 2021), accurate and timely forecasts of thunderstorm occurrence will become ever more important.

Thunderstorm forecasts based on the extrapolation of remote sensing data (nowcasts) become less reliable beyond an hour (Leinonen et al. 2023); therefore, numerical weather prediction (NWP) is often used for the longer lead times required in many critical decision-making processes. Invoking mathematical models and current observations, NWP simulates the future atmospheric state encoded in terms of meteorological variables (Bauer et al. 2015; Palmer 2017). In this study, we use a convection-permitting NWP model, which explicitly resolves convective processes without the need for convection parameterizations (Yano et al. 2018).

The identification of thunderstorms in NWP model output is complicated by the fact that no single variable directly indicates thunderstorm occurrence. Instead, one simultaneously considers multiple single-level predictors, which are derived from three-dimensional NWP variables and act as surrogate indicators of thunderstorm occurrence (Sobash et al. 2011; Kober et al. 2012; Simon et al. 2018). These predictors are motivated by a combination of experience, physical models, and domain knowledge. Examples include convective available potential energy (CAPE), precipitation rate, and relative humidity at 700 hPa. The occurrence of thunderstorms is inferred from these surrogate fields based on forecasters’ expertise. Recently,

---

*Corresponding author:* Kianusch Vahid Yousefnia, kianusch.vahidyousefnia@dlr.de

machine learning (ML) techniques have become increasingly popular for this purpose, leveraging methods such as fuzzy logic (Lin et al. 2012; Li et al. 2021), random forests (Herman and Schumacher 2018; Loken et al. 2020), and neural networks (Sobash et al. 2020; Geng et al. 2021; Zhou et al. 2022; Jardines et al. 2024), with the latter often proving more effective (Herman and Schumacher 2018; Ukkonen and Mäkelä 2019). ML involves training algorithms to recognize patterns and make predictions based on labeled data, which serve as the ground truth. For thunderstorm forecasting, these labels are often obtained from observational data sources such as lightning detection networks (Ukkonen and Mäkelä 2019; Geng et al. 2021) and radar imagery (Gagne et al. 2017; Burke et al. 2020). We recently introduced the feedforward neural network model SALAMA (Signature-based Approach of Identifying Lightning Activity Using Machine Learning), which infers the probability of thunderstorm occurrence from 21 NWP single-level predictors related to thunderstorm activity, outperforming classification based only on NWP reflectivity for lead times up to at least 11 h (Vahid Yousefnia et al. 2024).

Most single-level predictors can be derived from the vertical profiles of three-dimensional meteorological variables. For example, CAPE is determined by the vertical profiles of pressure, temperature, and specific humidity (Markowski and Richardson 2011). Thus, the information contained in a set of single-level predictors is inherently present in the corresponding vertical profiles, though in a more complex, encoded form. Consequently, an ML model trained directly on vertical profiles should, at a minimum, match the performance of one trained on single-level predictors. Given that a model based on vertical profiles has greater flexibility to detect patterns in NWP data, we hypothesize that such a model would outperform one using only single-level predictors—this is the primary focus of the present study.

In this work, we introduce SALAMA 1D, a deep neural network trained on vertical profiles of three-dimensional meteorological variables from a convection-permitting NWP model, bypassing the conventional use of single-level predictors. To our knowledge, this is the first study to apply neural networks directly to vertical profiles of convection-permitting forecasts for the purpose of predicting thunderstorm occurrence. We use data from ICON-D2-EPS (Zängl et al. 2015; Reinert et al. 2020), a convection-permitting NWP ensemble model for Central Europe with a horizontal resolution of  $\sim 2$  km and 65 vertical levels, operationally run by the German Meteorological Service (DWD). Lightning observations from the LINET detection network (Betz et al. 2009) serve as the ground truth. The design of SALAMA 1D is guided by physical principles. Specifically, a sparse layer reduces the number of parameters by promoting interactions within the same height levels, while a shuffling mechanism discourages the model

from learning patterns related to the vertical grid structure. This shuffling also acts as a form of regularization, helping to prevent overfitting. Our results demonstrate that SALAMA 1D achieves superior performance compared to the original SALAMA model, maintaining higher skill for lead times of up to at least 11 hours.

A major issue of ML models concerns the interpretability of their output. In this work, we conduct a sensitivity analysis using saliency maps to explore how the model interprets the input vertical profiles. This analysis reveals that our model primarily focuses on mesoscale patterns indicative of convection initiation, while also integrating insights from fine-grained processes related to ongoing convection. Our model effectively rediscovers characteristic tropospheric phenomena, aligning with established theoretical understandings of thunderstorm development and occurrence.

Our work demonstrates the potential of applying deep neural network models directly to complex, minimally processed input data, as opposed to relying on lower-dimensional, feature-engineered inputs fed into shallow ML models. Furthermore, we illustrate how incorporating physical constraints can enhance the model’s robustness and computational efficiency, while also emphasizing the importance of gaining interpretability—and thus trust—through techniques such as saliency maps. These advancements are particularly crucial for enabling ML models to reliably assist in critical decision-making processes in severe weather forecasting.

The structure of this work is as follows: In Section 2, we provide details on the NWP data used, the lightning observations, and the methodology for compiling ML training sets. Section 3 describes our ML model, including its architecture and training process. In Section 4, we report our results, including the sensitivity analysis, while Section 5 summarizes our work and elaborates on its implications with possible future research avenues.

## 2. Data

Our objective of data collection is to train an ML model for inferring the conditional probability of thunderstorm occurrence given an array  $\xi \in \mathbb{R}^{N_f \times N_z}$  of  $N_f$  meteorological variables at  $N_z$  height levels. The ML task is known as binary classification. ML models for this task are trained with examples. In our case, an example is a tuple  $(\xi, y)$ , where the label  $y \in \{0, 1\}$  denotes the class to which the example belongs (class 1: thunderstorm occurrence, class 0: no thunderstorm occurrence). In this section, we provide details on how we obtain  $\xi$  from NWP forecasts and  $y$  from lightning observations.

Data is collected for a region which encompasses Germany, as well as parts of its neighboring countries, as shown in Fig. 1. This region roughly corresponds to the NWP model domain, which we cropped at the borders

by approximately 80 km to reduce boundary computation errors.

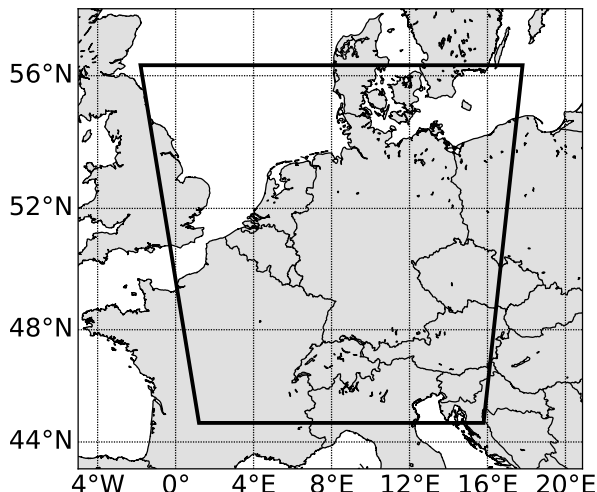


FIG. 1. Study region for this work, shown in a parallel projection. The polygon vertices are listed counterclockwise from the bottom-left: (44.7°N, 1.2°E), (44.7°N, 15.8°E), (56.3°N, 17.8°E), (56.3°N, 1.8°W)

#### a. NWP data

The operational runs of ICON-D2-EPS are initialized daily every 3 h, starting at 0000 UTC. For each full hour of the day, we collect only the latest (and, therefore, most accurate) available forecast, which is at most 2 h old. We gather forecasts for some summer months in 2021 (June, July, August), 2022 (May, June, July), and 2023 (July, August). ICON-D2-EPS comprises 20 ensemble members, which reflect the NWP uncertainty in the initial conditions, model error, and boundary conditions (Reinert et al. 2020). We collect the forecasts for all members of the ensemble system.

The  $N_f$  variables we extract from the forecasts are given in Table 1 and correspond to the fields that are operationally available in ICON-D2-EPS on vertical levels. We keep the fields on their native grid (vertically:  $N_z = 65$  non-equidistant levels, horizontally: spherical triangles) to avoid interpolation errors.

#### b. Lightning observations

In order to reconstruct the timing and location of past thunderstorm occurrences in our study region, we consult observation data from the lightning detection network LINET (Betz et al. 2009). We choose lightning observations as the ground truth for thunderstorm occurrence due to their high and uniform detection efficiency ( $\geq 95\%$  for LINET) and spatial accuracy (150 m for LINET), similarly to Ukkonen and Mäkelä (2019); Vahid Yousefnia et al. (2024).

TABLE 1. (Instantaneous) vertical ICON-D2-EPS field profiles used in this study.

ICON variable	Description
U	Zonal wind speed
V	Meridional wind speed
T	Temperature
P	Pressure
QV	Specific humidity
QC	Cloud water mixing ratio
QI	Cloud ice mixing ratio
QG	Graupel mixing ratio
CLC	Cloud cover
W	Vertical wind speed

Given an NWP grid point at horizontal position  $\mathbf{x}$  and time  $t$ , we consider a thunderstorm to occur at  $(\mathbf{x}, t)$  if a flash of lightning is detected at any  $\mathbf{x}_l, t_l$  with

$$\|\mathbf{x} - \mathbf{x}_l\| < \Delta r \quad \text{and} \quad |t - t_l| < \Delta t, \quad (1)$$

where  $\|\cdot\|$  denotes the great-circle distance between  $\mathbf{x}$  and  $\mathbf{x}_l$  on a perfect sphere of the Earth with a radius of 6371.229 km, as assumed in the ICON-D2-EPS model (Reinert et al. 2020). The spatial and temporal thresholds used in this study read  $\Delta r = 15$  km and  $\Delta t = 30$  min. NWP models struggle with accurately predicting the correct location and timing of convection (Roberts and Lean 2008); therefore, grid points with a positive class label do not reliably coincide with convective patterns in the NWP model. As our model is designed to postprocess NWP forecasts, its skill is in turn fundamentally limited by NWP forecast uncertainty. We revisit this issue in Section b.

#### c. ML data set compilation

NWP data and lightning observations are combined to tuples  $(\boldsymbol{\xi}, y)$ . Here,  $\boldsymbol{\xi}$  denotes the NWP profiles for one ensemble member at a particular grid point and time, and  $y$  denotes the corresponding ground truth. This results in a collection of tuples, from which we randomly draw elements to compile three pairwise disjoint data sets. A training set ( $4 \times 10^5$  tuples) is used to train the ML model. A validation set ( $10^5$  tuples) is used to monitor training progress and decide when to stop training. Finally, ML model skill is measured using a test set ( $10^5$  tuples) with data that the model has not seen during training. In order to examine whether extending the study period from which to gather examples enhances skill, we compile two training sets: one contains examples from 2021 and 2022, while the other one is made up of examples from only 2021.

To reduce correlations between the data sets, we ensure temporal separation, which is common practice (Ravuri

et al. 2021; Geng et al. 2021; Jardines et al. 2024). While examples from 2022 and/or 2021 are used for training, the examples from 2023 are divided among the test and validation set as follows: Even days of the month are test days and odd ones are validation dates. However, if a developed thunderstorm persists after 0000 UTC, this could introduce correlations between the test set and the validation set. To minimize the occurrence of this, we let each day begin at 0800 UTC, as in Vahid Yousefnia et al. (2024). This time of the day has been identified in the collected lightning data as the hour of least lightning activity.

An issue that arises is high class imbalance (observing the class “thunderstorm occurrence” is climatologically less likely than observing the opposite class). In order to estimate the relative frequency  $g$  of thunderstorm occurrence expected for the test set, we evaluate lightning observations for July and August from 2018 to 2022. We obtain  $g = 0.0193(23)$ , the uncertainty showing the symmetric 90% confidence interval. The problem with such a small value of  $g$  is that the model might not see enough examples of the minority class during training to learn meaningful patterns. To ensure that the model is presented with sufficiently many positive examples, we compile a class-balanced training set by randomly undersampling the majority class, as is common practice (Hasanin and Khoshgoftaar 2018; Mohammed et al. 2020; Vahid Yousefnia et al. 2024). The validation and test set, however, are compiled in a climatologically consistent manner. The reason for this choice is to ensure that we evaluate our model in a realistic setting in which thunderstorms rarely occur. When a model trained on balanced data is used with climatologically consistent data sets, we need to calibrate the raw model output  $p'$  using the following formula to obtain a well-calibrated probability  $p$  (Vahid Yousefnia et al. 2024):

$$p = \frac{gp'}{gp' + (1-g)(1-p')} \quad (2)$$

### 3. Methods

In this section, we present the architecture used for SALAMA 1D and give training details. In addition, we introduce an ML baseline model that infers thunderstorm occurrence from derived single-level predictors.

#### a. Model description

Given an input sample  $\xi$  of NWP predictors (for a given member, grid point, and forecast time), we aim to develop a model that predicts the corresponding probability of thunderstorm occurrence. Our model constitutes a lead-time-independent post-processing framework for NWP forecasts. To obtain, for example, an 8-hour forecast of the probability of thunderstorm occurrence, one needs to apply our model to an 8-hour forecast of NWP predictors. While we train on forecasts with a lead time of at most 2 h,

in Section 4 we examine whether the patterns learned by the ML model generalize to longer lead times.

We use an artificial neural network model  $\mathbb{R}^{N_f \times N_z} \rightarrow (0, 1)$  to describe the relationship between the input sample  $\xi$  and the corresponding probability of thunderstorm occurrence. The architecture of SALAMA 1D, as illustrated in Fig. 2, combines dense layers with a sparse layer strategically designed to reduce the number of parameters and eliminate unnecessary connections. This approach addresses challenges such as overfitting and the high computational demands typically associated with large ML models. Instead of using the pruning technique (LeCun et al. 1989; Frankle and Carbin 2019), we incorporate physical considerations and symmetry considerations to achieve a reduction in parameters. Because translational symmetry is broken along the  $z$ -direction, weight sharing, as in convolutional layers, cannot be applied effectively. Instead, we implement sparse connections, allowing interactions only between field values at similar height levels (Section b). Dense layers further downstream then construct more complex dependencies between more distant field values. Additionally, we introduce a shuffling mechanism to ensure that the model does not rely on the vertical grid structure, forcing it to infer orientation from the data itself. This design allows the model to, for instance, associate the formation of ice particles with the height of the tropopausal temperature inversion rather than a fixed height level, such as level 11. It turns out that shuffling also regularizes the model, limiting overfitting issues further.

Training is then performed analogously to Vahid Yousefnia et al. (2024): We scale the input fields to have zero mean and unit variance before minimizing binary cross-entropy loss via the Adam optimizer (Kingma and Ba 2014). Training is stopped when validation loss no longer decreases. Equation (2) is applied with the sample climatology value found in Section 2 whenever the model is used on climatologically consistent data sets.

#### b. Sparse connections

In this section, we provide technical details on the sparse layer implementation. The input layer is given by an array of shape  $(N_f, N_z)$  with a field dimension (iterating over the  $N_f$  field profiles) and a height dimension (iterating over the  $N_z$  vertical levels). Now, we consider a block of shape  $(N_f, k)$ , where  $k$  is the size of the block along the height dimension. We densely connect the nodes within this block to  $h$  nodes in the following layer. Next, we slide the block by  $s$  nodes along the height dimension and, again, densely connect the corresponding nodes to  $h$  subsequent nodes of the following layer. This is schematically shown in Fig. 3. Starting with a block at the bottom of the input layer, we repeat this procedure until reaching the top of the input layer. Provided that  $N_z - k$  is divisible by  $s$ , this procedure leads to  $N_k = (N_z - k + s)/s$  blocks and produces  $N_k \cdot h$

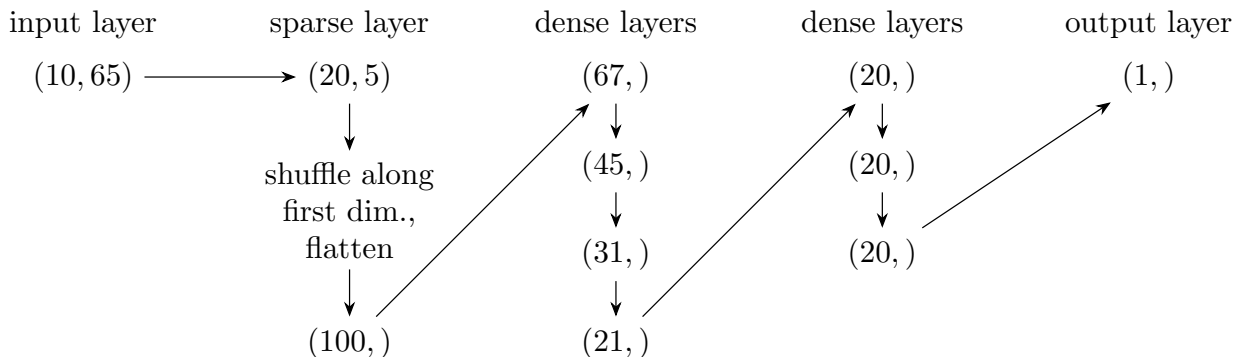


Fig. 2. Change in input size during a forward pass in SALAMA 1D. The sparse layer (Section b) reduces dimensionality and shuffles the data to prevent the model from learning dependencies tied to the vertical grid structure. Additionally, the shuffling acts as a regularization technique, helping to limit overfitting. Input fields are scaled to order 1. We use rectified linear units as activation functions after the flattened sparse layer and each dense layer, and a sigmoid function to map the output layer to the open interval  $(0, 1)$ . The sparse layer has 8100 trainable parameters, the other layers add 13226 parameters.

nodes in the following layer. We incorporate a shuffling mechanism that randomly permutes the order of the blocks for each example during training.

In contrast to a convolutional layer with a sliding kernel, all  $N_k$  blocks in our sparse layer have their own set of free parameters. In total, the sparse layer contributes  $N_k \cdot (N_f \cdot k + 1) \cdot h$  to the model. We have studied a large variety of  $(k, s, h)$ -combinations and found that skill depends barely on the particular sliding block configuration as long as a sufficiently large number of parameters is exceeded. Setting  $k = 8, s = 3, h = 5$ , which corresponds to the smallest model configuration with saturating skill, we obtain  $N_k = 20$  blocks, and 8100 trainable parameters. In comparison to a fully dense layer, the parameter size is reduced by around 90%.

### c. Baseline model

In order to study the potential benefit of post-processing vertical NWP profiles instead of derived single-level predictors, we implement the ML model from Vahid Yousefnia et al. (2024), which we refer to as SALAMA 0D in the following (in contrast to SALAMA 1D, which processes one-dimensional vertical profiles). SALAMA 0D uses a set of 21 established predictors related to thunderstorm activity to infer calibrated probabilities of thunderstorm occurrence. The predictors are mapped to a single node via three dense layers with 20 nodes each. In fact, the architectures of SALAMA 0D and SALAMA 1D are identical in the last five layers (Fig. 2). Both models operate point by point, which allows for a direct and fair comparison. We retrain SALAMA 0D with training data from 2021 which matches the NWP model, the study region, and study period, used for SALAMA 1D. In contrast to the original paper, we feed the NWP data to SALAMA 0D on

its native horizontal grid, reducing potential interpolation errors.

## 4. Results

We intend to investigate two aspects concerning the model skill of SALAMA 1D. Firstly, we compare SALAMA 1D to the introduced baseline model, studying the potential benefit of considering vertical profiles (instead of derived single-level predictors) for the prediction of thunderstorm occurrence. On the other hand, we are interested in examining whether extending the study period from which to gather training examples enhances skill. Therefore, we show the results for two configurations of SALAMA 1D:

- SALAMA 1D-2021: SALAMA 1D, trained with data from 2021.
- SALAMA 1D-2022: SALAMA 1D, trained with data from 2021 and 2022.

The baseline model, SALAMA 0D, has been trained with data from 2021; it can, therefore, be readily compared with SALAMA 1D-2021. Note that while SALAMA 1D-2022 is trained on data from a longer study period than the two other models, the size of the training set does not change. Potential improvements in skill with respect to SALAMA 1D-2021 can, therefore, be unambiguously attributed to increased data variability. The results from the model comparison are given in Section a. Furthermore, we study how sensitively SALAMA 1D-2022 reacts to small input changes. The results, shown in Section b, offer insight into how the model infers thunderstorm occurrence from the input.

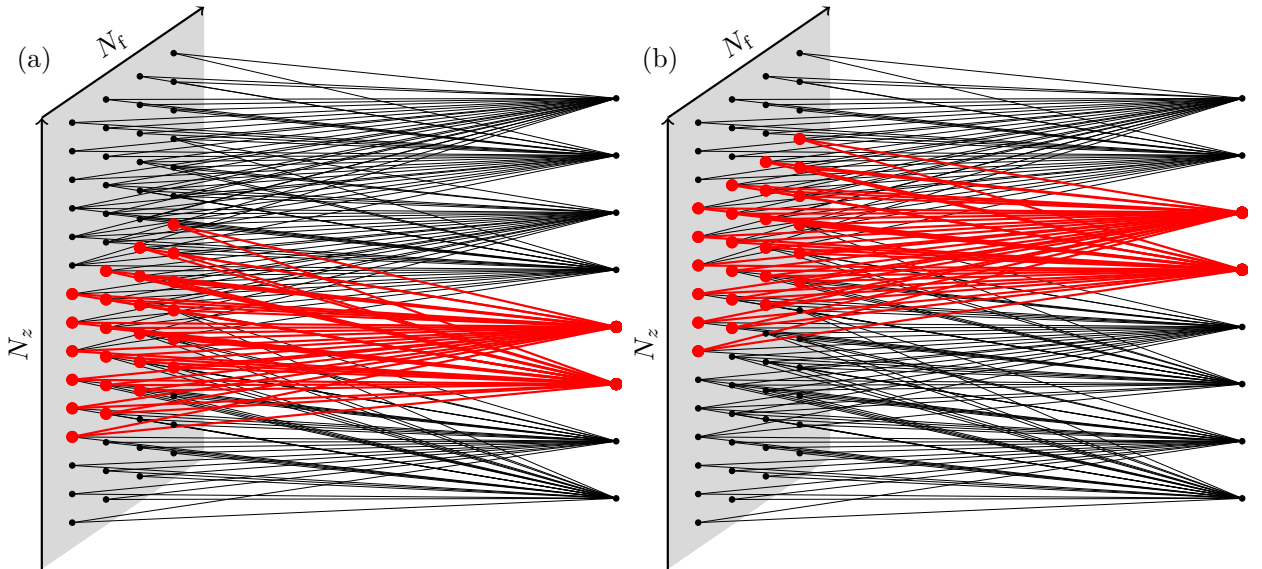


Fig. 3. Illustration of the connections (thick lines between bold dots) between the input layer of shape  $(N_f, N_k)$  and the following layer. The input layer is shown in two dimensions to help visualize each vertical field profile, but there is no spatially extended structure beyond the vertical ( $z$ ) direction. (a) A block of nodes of shape  $(N_f, k)$  in the input layer is connected to  $h$  nodes in the following layer. (b) Then, the block is shifted upwards by  $s$  nodes and rewired with the next  $h$  nodes of the following layer.

#### a. Model comparison

In order to get a first idea of the skill of the three models, we consider two cases with thunderstorm activity in Central Europe, namely July 24, 2023, 2200 UTC (case A), and August 2, 2023, 1200 UTC (case B). These two cases were chosen since they display multiple simultaneous convective regions of varying size. In Fig. 4, we show maps of the probability of thunderstorm occurrence for Central Europe as produced by the three models and compare them with lightning observations. The probability maps have been computed by retrieving the latest NWP forecast for each target time (case A: the 2-hour forecast of the 1500 UTC model run, case B: 0-hour forecast of the 1200 UTC run) and applying the SALAMA models to them. The ML models can be applied to all NWP ensemble members, producing separate probability output for each member. We show the results for only a single member.

Case A is characterized by intense thunderstorm activity from the Alps to Northern Germany, with roughly ten convective objects of different sizes. Most lightning contours are predicted by all three models. However, SALAMA 0D produces a significant number of false alarms. SALAMA 1D-2021 corrects many of them, especially in Southern Germany. SALAMA 1D-2022 tends to make its predictions more confidently than the other models, resulting in more contours that are filled out with high-probability pixels. On the other hand, the model seems to produce slightly more false alarms than SALAMA 1D-2021.

Thunderstorm activity in case B occurs primarily over the Benelux, while two smaller thunderstorms are observed

over the North Sea. The latter two events are missed by the three models, though SALAMA 1D-2022 only misplaces the storms towards the South. The thunderstorm over the Benelux is captured to some extent by all the models. However, the SALAMA 1D models are more confident in their predictions, producing high-probability pixels almost everywhere within the thunderstorm contour. On the other hand, they overestimate the size of the thunderstorm, resulting in false alarms directly outside the contour. SALAMA 0D predicts a wide band of thunderstorm activity over France and Southwestern Germany, which was not confirmed by lightning observations. This region of false alarms is significantly reduced by the two SALAMA 1D models, with SALAMA 1D-2022 reducing the region to essentially zero.

To compare the models quantitatively, we use the test set from Section 2. The first instrument we use for comparing model skill is a reliability diagram (Wilks 2011; Bröcker and Smith 2007). Partitioning the range  $(0, 1)$  of possible model probabilities into  $N_b$  equidistant bins, we distribute the test examples among the bins according to the model probability they have been assigned. For each bin  $i = 1, 2, \dots, N_b$ , we extract the observed relative frequency  $\bar{o}_i$  of thunderstorm occurrence, the bin-averaged model probability  $p_i$ , and the number  $N_i$  of examples per bin. A reliability diagram then consists of a calibration function and a refinement distribution. The calibration function is a plot of  $\bar{o}_i$  against  $p_i$ , and measures whether the model probabilities are consistent with the observed relative frequency of thunderstorm occurrence, a charac-



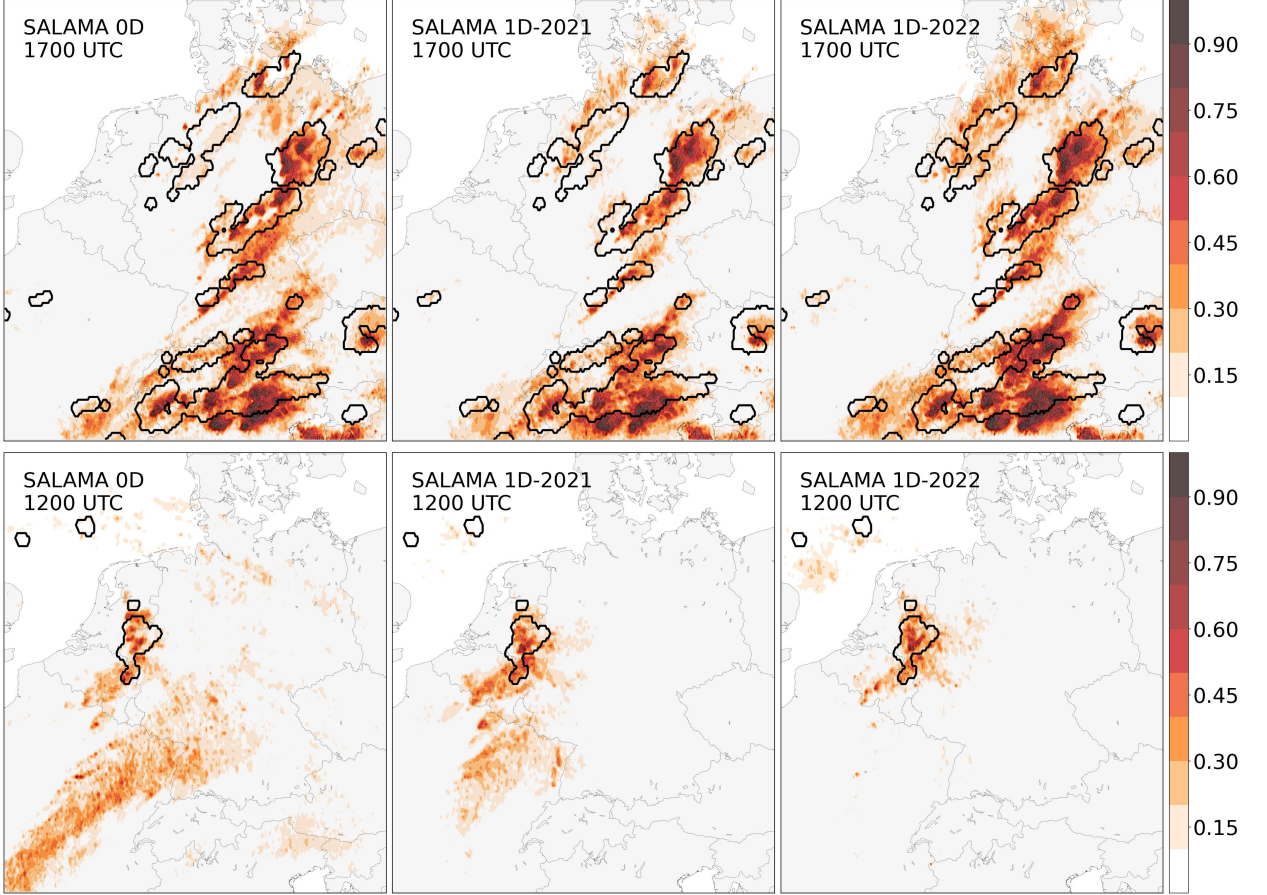


FIG. 4. Model probability of thunderstorm occurrence for the three models of this study, evaluated for July 24, 2023, 1700 UTC (upper panels), and August 2, 2023, 1200 UTC (lower panels). The filled contours with varying shading display the result for the first ensemble member of ICON-D2-EPS, whereas lightning labels (Section 2) are shown as black contours. None of the dates have been used for training. NWP forecast lead times are 2 h for the upper panels and 0 h for the lower panels.

teristic known as reliability. A well-calibrated model exhibits a calibration function close to the 1:1 diagonal. The refinement distribution corresponds to the distribution of model probabilities. Skillful models are capable of producing well-calibrated model probabilities larger than climatology, which is referred to as resolution.

In the upper panels of Fig. 5, we show for each of our models the corresponding reliability diagram with  $N_b = 10$  bins. All models display a similar degree of high reliability. We reiterate here that it is important to apply the analytic model calibration (2), otherwise high reliability could not be expected. The refinement distributions, as well, look similar. However, the model resolutions differ significantly: Following Vahid Yousefnia et al. (2024), we introduce the bin-wise contributions to reliability and

resolution

$$\text{RES}_i = \frac{1/\Delta p_i}{g(1-g)} \frac{N_i}{N} (p_i - g)^2, \quad (3)$$

$$\text{REL}_i = \frac{1/\Delta p_i}{g(1-g)} \frac{N_i}{N} (p_i - \bar{o}_i)^2, \quad (4)$$

where  $\Delta p_i = 1/N_b$  denotes bin width. The area between  $\text{RES}_i$  and  $\text{REL}_i$  as a function of  $p_i$  serves as a positively-oriented measure of skill. According to Murphy (1973), this area is equivalent to the Brier skill score (BSS). The lower panels of Fig. 5 display bin-wise reliability and resolution, revealing that the increase in skill, measured by the BSS, for the two SALAMA 1D models is attributed to improved resolution. For SALAMA 1D-2021, both low- and high-probability examples enhance resolution, while for SALAMA 1D-2022, all bins with  $p_i > 0.3$  contribute additional improvements to resolution.

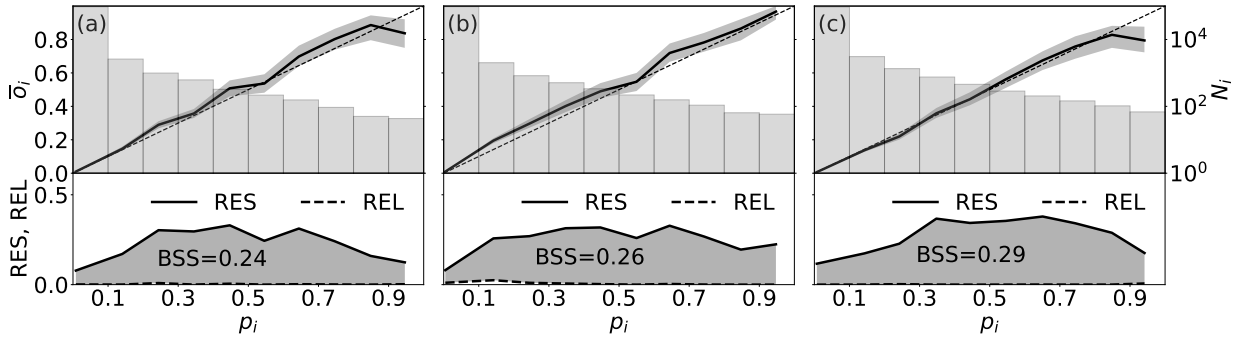


Fig. 5. Reliability diagram for (a) SALAMA 0D, (b) SALAMA 1D-2021, (c) SALAMA 1D-2022. Upper panels show the calibration curve and the refinement distribution, while the lower panels display bin-wise resolution and reliability (Eqs. (3) and (4)). The enclosed area corresponds to the Brier Skill Score (BSS).

In Table 2, we summarize the performance of the three models using several additional skill scores established for problems with class imbalance (Wilks 2011; Saito and Rehmsmeier 2015; Vahid Yousefnia et al. 2024). These scores are positively oriented and bounded by unity. Across all skill scores, the SALAMA 1D models consistently outperform SALAMA 0D, with SALAMA 1D-2022 showing higher skill than SALAMA 1D-2021. It is also noteworthy that the inference time is comparable for all models; thus, the SALAMA 1D models are equally well-suited for real-time operational use, in addition to offering superior skill compared to SALAMA 0D.

So far, we have worked with a test set that consists of examples from NWP forecasts with a lead time of at most 2 h (Section 2). Next, we examine systematically how model skill depends on NWP forecast lead time. For this purpose, we generate test sets in which the examples result from NWP forecasts with a fixed lead time. As before, the position within the study region, the ensemble member index, and hour of the day, are randomly drawn from uniform distributions. The target times are drawn from the same test days as in Section 2.

The lead-time dependence of skill is shown in Fig. 6. While we measure skill in terms of the BSS, we have checked that the results of this section do not qualitatively change when considering a different skill score. All three models exhibit an approximately exponential decrease in skill. The rate at which skill decreases is very similar for the three models. This suggests that the decrease of skill is not model-specific but results from an increasing NWP forecast uncertainty, which is consistent with previous work (Vahid Yousefnia et al. 2024). As a consequence, the SALAMA 1D models' superior skill for low lead times is passed on to longer lead times.

It is worth noting that the decrease in skill of SALAMA 0D is stronger than reported in Vahid Yousefnia et al. (2024). There, initial skill decreased by at most 30% after 11 h, while the decrease here is approximately twice as much. This may result from using more diverse test sets

in this study (we use twice as many test days to compile the training set). Furthermore, we do not apply any horizontal interpolation for compiling data sets in the present work, possibly allowing the model to rely on gridscale structures that would otherwise be masked by interpolation errors.

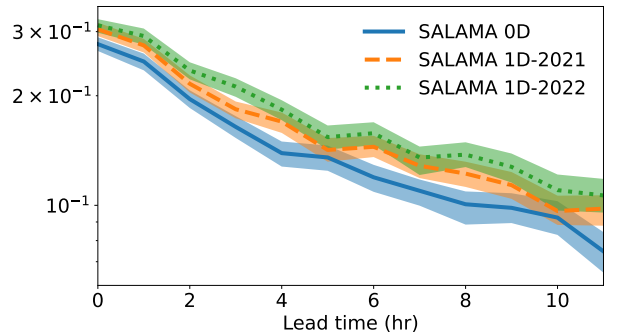


Fig. 6. Lead-time dependence of model skill (quantified by the BSS). Uncertainties are obtained from 200 bootstrap resamples and show the symmetric 90% confidence interval.

### b. Sensitivity analysis

For the remainder of this section, we focus on SALAMA 1D-2022, referring to it simply as SALAMA 1D. In order to gain insight into how, given an input sample  $\xi$ , the conditional probability  $f$  of thunderstorm occurrence (SALAMA 1D model output) is inferred, we conduct a linear sensitivity analysis. For this purpose, we consider for a given scaled (Section 3) input sample  $\xi = (\xi_{ij}) \in \mathbb{R}^{N_f \times N_z}$  the partial derivatives of  $f$ :

$$S_{ij}(\xi) \equiv \left| \frac{\partial f(\xi)}{\partial \xi_{ij}} \right| \quad (5)$$

The term  $S_{ij}(\xi)$  constitutes a measure of how much  $f$  reacts to changes in  $\xi_{ij}$  and, therefore, quantifies the importance of  $\xi_{ij}$  to the outcome.  $S_{ij}(\xi)$  is commonly referred



TABLE 2. Scores for classification skill, as defined in e.g. Vahid Yousefnia et al. (2024), evaluated on the test set. All scores except BSS and PR-AUC require setting a decision threshold to convert probabilities to binary output. The threshold is chosen such that the average fraction of examples classified as thunderstorms is equal to the observed fraction of thunderstorm examples, and amounts to 0.211 (SALAMA 0D), 0.193 (SALAMA 1D-2021), 0.264 (SALAMA 1D-2022). Uncertainties are obtained from 200 bootstrap resamples and show the symmetric 90% confidence interval.

	Skill score	0D	1D-2021	1D-2022
Brier skill score (BSS)		0.239(12)	0.264(12)	0.288(14)
Area under the precision–recall curve (PR-AUC)		0.400(19)	0.446(18)	0.459(21)
	Recall	0.430(17)	0.453(16)	0.472(19)
	Precision	0.430(17)	0.453(14)	0.471(17)
	$F_1$ -score	0.431(15)	0.453(14)	0.471(17)
Critical success index (CSI)		0.274(12)	0.293(12)	0.308(14)
Equitable threat score (ETS)		0.263(12)	0.282(12)	0.288(14)

to as saliency in the ML literature (Simonyan et al. 2014; Li et al. 2022) while meteorologists might know it as adjoint sensitivity (Errico 1997; Warder et al. 2021).

Saliency varies from example to example and is used to interpret individual predictions. In order to gain more general insight, we propose considering statistical averages over suitable sets of examples. In the following, we evaluate saliency for the top and bottom probability percentile of test set examples. The resulting saliency maps characterize how SALAMA 1D tends to infer high and low probabilities of thunderstorm occurrence, respectively. We present them in Fig. 7 and Fig. 8, together with the corresponding average field profiles. Note that average saliencies of the different fields are stacked on top of each other. As a consequence, the saliency envelope quantifies how much individual height levels affect the model outcome. Average field profiles are shown in the same color as the corresponding average saliency. We left out the average pressure profile as it displays for both percentiles the same monotonically decreasing dependence of height, suggesting that pressure is essentially hydrostatic.

Beginning with the top percentile, we find one dominating peak at a height of  $z \approx 5$  km, and a smaller one at  $z \approx 12$  km. The large peak is almost entirely made up of contributions from temperature and pressure. To understand this, note that the model is not explicitly informed about the height of individual vertical levels; rather, these levels are randomly shuffled (Section 3). Due to the shuffling, we expect the pressure profile saliency to become a proxy for how much the model relies on vertical gradients. This is because hydrostatic pressure monotonically decreases with height and, therefore, contains information about vertical level spacings. Hence, the large peak suggests that the model reconstructs temperature lapse rates at the peak level. Additionally, Fig. 7 shows the average level of free convection (LFC) and equilibrium level (EL) for a mixed-layer parcel. The large peak is bounded by the LFC and the EL, which suggests that mixed-layer parcels

are buoyant for heights in the vicinity of this peak. Positive buoyancy occurring in a conditionally unstable troposphere is known to be a crucial ingredient for thunderstorm development (Doswell et al. 1996) and is the basis for several traditional thunderstorm predictors, e.g. convective available potential energy. Conditional instability significantly depends on the environmental temperature lapse rate, which is consistent with temperature and pressure displaying high saliency between the LFC and the EL.

The highest-altitude peak closely coincides with the tropopause, which we see by computing the average tropopause height according to the WMO definition (World Meteorological Organization 1957). While this peak receives similar contributions from different fields, the saliency of the cloud ice mixing ratio (QI) is maximal at this level. QI is present only at this height, as seen from the profile of average QI. This shows that the model actively takes ice particle content into consideration to infer thunderstorm occurrence. On the other hand, the model does not consider graupel content (QG) equally much. Presumably, this is because QG is maximal between the LFC and the EL, where the model has identified with the temperature lapse rate a more effective proxy for thunderstorm activity. As for specific humidity (QV), our study shows that the saliency of QV is highest around the LFC. Comparing the dew point profiles shows that high-probability examples exhibit more low-level moisture than low-probability examples. This supports the importance of low-level moisture for thunderstorm development, as dry air mixing in with rising air parcels reduces their buoyancy (Doswell et al. 1996; Markowski and Richardson 2011).

Next, we turn to the bottom 1% of examples. Note that the model is far less sensitive to input variability for the bottom class than for the top class—average saliency is roughly five orders of magnitude smaller. Nevertheless, average saliency varies as a function of height and field, displaying three distinct peaks. The upper two peaks coincide with those of the top class, though the contributions

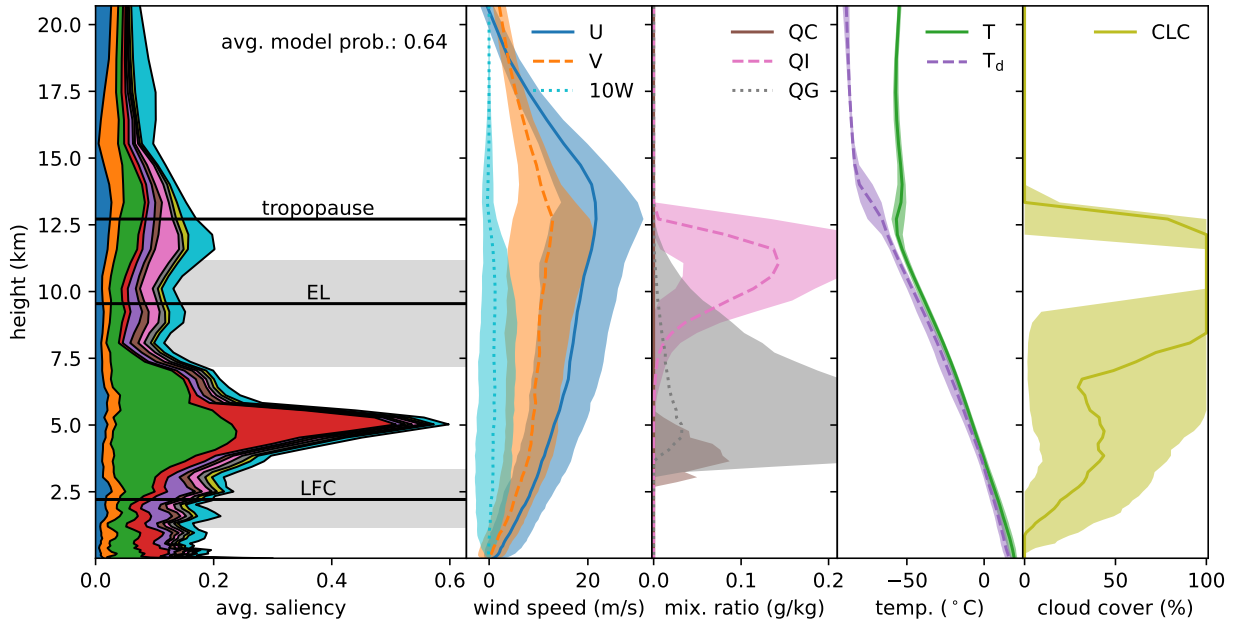


FIG. 7. Average saliency plotted against height for the top percentile of test set examples (based on model probability), with annotated levels of the tropopause, LFC, and EL (left panel), and corresponding average field profiles (remaining panels). We convert average specific humidity to dew point temperature  $T_d$  for a comparison with  $T$ . The average pressure profile is not shown as it appears to be essentially hydrostatic. Shaded bands correspond to the symmetric 50% confidence interval. Saliencies for the different fields are stacked on top of each other in the order given in Table 1 (the colors used for average saliency match those for the average field profiles).

to the middle peak slightly change: The water quantities QC, QI, QG, as well as cloud cover (CLC) and vertical velocity ( $W$ ) contribute more to this peak than for the top class. The profiles of these variables vanish in the vicinity of the middle peak for the bottom class but not for the top class, which suggests that the model infers thunderstorm occurrence from the absence of these fields.

The bottom class features an additional low-level peak at  $z \approx 1$  km, which receives most contribution from temperature and pressure. As discussed before, this indicates that the model reconstructs a temperature lapse rate there, as well. Stable stratification in the lower troposphere is a known obstacle that parcels in the boundary layer need to overcome for thunderstorm development (Doswell et al. 1996). The energy required to overcome the barrier in parcel theory is given by convective inhibition. It depends on temperature, pressure, and specific humidity, which aligns with the composition of the peak.

A comparison between the CLC profiles of the two classes shows that the model associates non-vanishing cloud cover with a high probability of thunderstorm occurrence. In particular, close to the EL, CLC tends to be 100%. This is consistent with anvil cloud top levels (Markowski and Richardson 2011). Furthermore, it is noteworthy that high-probability examples tend to have northeastward wind profiles, whereas examples from the bottom class display southeastward winds. This is con-

sistent with studies on the typical propagation direction of thunderstorms in Central Europe (Hagen and Finke 1999).

The dominance of peaks related to environmental lapse rates and low-level moisture suggests that SALAMA 1D identifies thunderstorm occurrence essentially by patterns characteristic of convection initiation. These are typically mesoscale (Markowski and Richardson 2011). Only to a lesser extent is model outcome affected by fine-grained (sub-mesoscale) patterns representative of ongoing convection, such as vertical velocity and liquid/ice particle content. This might seem surprising as we use simulation data from an NWP model capable of producing realistic-looking convection. However, predicting the correct location and timing of convection remains challenging for convection-permitting NWP models (Roberts and Lean 2008). Therefore, SALAMA 1D may have learned to be cautious about fine-grained patterns if they do not reliably match lightning observations. As a result, it prefers larger-scale patterns, even though these broader structures can lead to more false alarms.

## 5. Discussion and conclusion

Bypassing the traditional use of derived single-level predictors from NWP data, we developed SALAMA 1D, an ML model for predicting the probability of thunderstorm occurrence on a pixel-wise basis by processing vertical

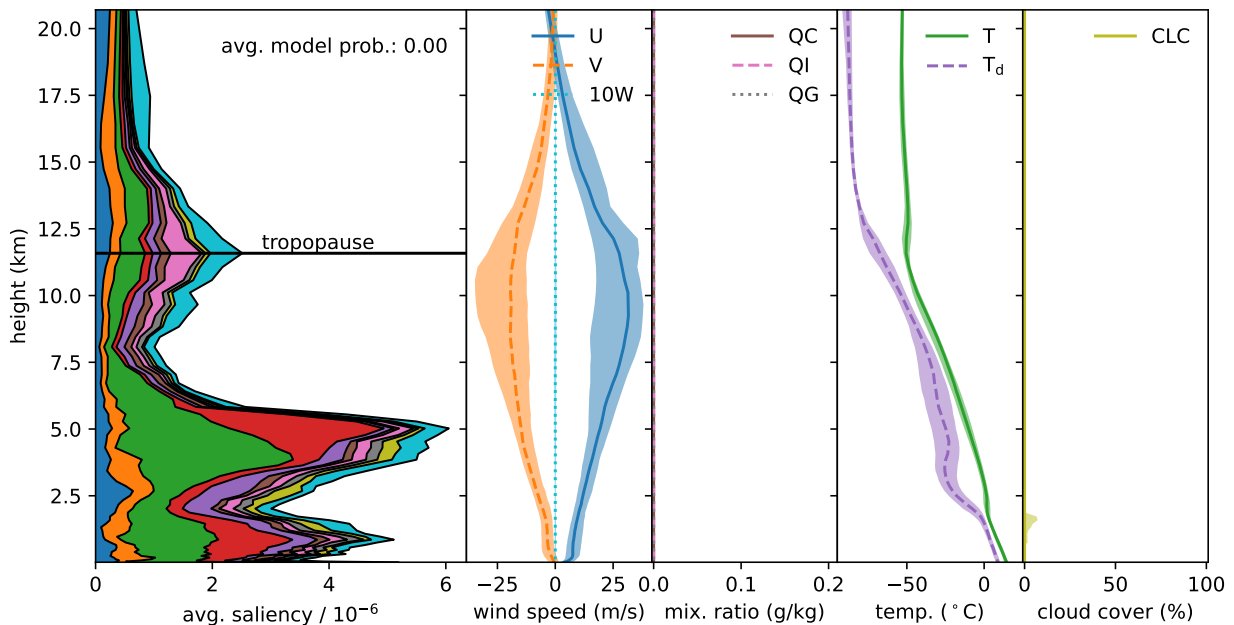


Fig. 8. Average saliency plotted against height for the bottom percentile of test set examples (based on model probability), with annotated levels of the tropopause (left panel), and corresponding average field profiles (remaining panels). Temperature profiles are not conditionally unstable for this class, so there is no LFC or EL. We convert average specific humidity to dew point temperature  $T_d$  for a comparison with  $T$ . The average pressure profile is not shown as it appears to be essentially hydrostatic. Shaded bands correspond to the symmetric 50% confidence interval. Saliencies for the different fields are stacked on top of each other in the order given in Table 1 (the colors used for average saliency match those for the average field profiles).

profiles of three-dimensional variables from convection-permitting NWP forecasts. The model’s architecture was motivated by physical considerations. In particular, a sparse layer reduced parameter size by encouraging interactions at similar height levels, while a shuffling mechanism prevented the model from learning patterns tied to the vertical grid structure. The latter also added a form of regularization that limited overfitting.

In comparison to SALAMA 0D, an ML baseline model that infers thunderstorm occurrence from derived single-level features, our model demonstrated higher skill across a wide range of metrics and for lead times up to at least 11 h. This result indicates that information relevant to thunderstorm occurrence, while intricately encoded in vertical profiles, can be successfully extracted by machine learning, resulting in an improved ability to recognize thunderstorm occurrence in NWP forecasts. Notably, our model achieves this enhanced skill with only a modest increase in computational time during prediction, making it equally suitable for real-time operational use as SALAMA 0D. Furthermore, doubling the number of days used to compile the training set (while keeping the training set size constant) also increased skill, underscoring the importance of a large and diverse database of NWP data. We anticipate further skill improvements with the collection of more NWP data.

A sensitivity analysis based on saliency maps indicated that our model prioritizes temperature and pressure to reconstruct environmental lapse rates, possibly in order to infer levels of positive buoyancy and convection inhibition. Additional information is gathered from ice particle content near the tropopause, while the absence of mid-level graupel and cloud cover is used to rule out thunderstorm occurrence. The model relies significantly on mesoscale structures related to convective initiation, such as lapse rates and low-level moisture, and to a lesser extent on fine-grained structures characteristic of ongoing convection. We hypothesized that this preference arises because larger-scale patterns are more reliable for identifying thunderstorm occurrence, as fine-grained patterns may not consistently align with lightning observations due to the convection-permitting NWP model struggling to accurately predict the location and timing of convection. To encourage the use of fine-grained structures, it may be beneficial to train the model in such a way that it can process all ensemble members simultaneously in one forward pass. By analyzing the number of members displaying fine-grained signs of thunderstorm activity, the model could learn the degree to which it can trust the convection produced by NWP.

In closing, we stress that the methodology applied in this work may be useful for machine learning (ML) topics

beyond the identification of thunderstorm occurrence in NWP data. Our approach demonstrates how incorporating physical constraints and symmetry principles can lead to more robust and computationally efficient ML models. Additionally, our use of saliency maps highlights a path toward more interpretable ML models, fostering greater trust as we gain insight into how models arrive at their predictions. As ML continues to play a growing role in severe weather forecasting, ensuring that these models are both accurate and transparent will be key to enhancing their operational utility in critical decision-making processes.

*Acknowledgments.* We gratefully acknowledge the computational and data resources provided through the joint high-performance data analytics (HPDA) project ”terabyte” of the DLR and the Leibniz Supercomputing Center (LRZ). We thank Björn Brötz and Hessel Juliust for reviewing the ML code.

*Data availability statement.* We aim to make the training, validation, and testing datasets generated in this study publicly available on Zenodo, pending agreement with the lightning data provider. Negotiations regarding data sharing are currently ongoing. Additionally, we plan to release the code for all ML models as open source on GitHub, subject to authorization. The original simulation data from the ICON-D2-EPS model is accessible through the corresponding DWD database (<https://www.dwd.de/EN/ourservices/pamore/pamore.html>). Please note that the original data from the LINET lightning detection network is proprietary and cannot be shared in its raw form.

## References

- Bauer, P., A. Thorpe, and G. Brunet, 2015: The quiet revolution of numerical weather prediction. *Nature*, **525** (7567), 47–55.
- Betz, H. D., K. Schmidt, P. Laroche, P. Blanchet, W. P. Oettinger, E. Defer, Z. Dziewit, and J. Konarski, 2009: Linet—an international lightning detection network in europe. *Atmospheric Research*, **91** (2), 564–573, <https://doi.org/https://doi.org/10.1016/j.atmosres.2008.06.012>.
- Borsky, S., and C. Unterberger, 2019: Bad weather and flight delays: The impact of sudden and slow onset weather events. *Economics of Transportation*, **18**, 10–26, <https://doi.org/https://doi.org/10.1016/j.ecotra.2019.02.002>.
- Bröcker, J., and L. A. Smith, 2007: Increasing the reliability of reliability diagrams. *Weather and Forecasting*, **22** (3), 651–661, <https://doi.org/10.1175/WAF993.1>.
- Burke, A., N. Snook, D. J. G. II, S. McCorkle, and A. McGovern, 2020: Calibration of machine learning–based probabilistic hail predictions for operational forecasting. *Weather and Forecasting*, **35** (1), 149–168, <https://doi.org/https://doi.org/10.1175/WAF-D-19-0105.1>.
- Diffenbaugh, N. S., M. Scherer, and R. J. Trapp, 2013: Robust increases in severe thunderstorm environments in response to greenhouse forcing. *Proceedings of the National Academy of Sciences*, **110** (41), 16 361–16 366, <https://doi.org/10.1073/pnas.1307758110>, <https://www.pnas.org/doi/pdf/10.1073/pnas.1307758110>.
- Doswell, C. A., H. E. Brooks, and R. A. Maddox, 1996: Flash flood forecasting: An ingredients-based methodology. *Weather and Forecasting*, **11** (4), 560–581, [https://doi.org/10.1175/1520-0434\(1996\)011<0560:FFFAIB>2.0.CO;2](https://doi.org/10.1175/1520-0434(1996)011<0560:FFFAIB>2.0.CO;2).
- Errico, R. M., 1997: What is an adjoint model? *Bulletin of the American Meteorological Society*, **78** (11), 2577–2592, [https://doi.org/10.1175/1520-0477\(1997\)078<2577:WIAAM>2.0.CO;2](https://doi.org/10.1175/1520-0477(1997)078<2577:WIAAM>2.0.CO;2).
- Frankle, J., and M. Carbin, 2019: The lottery ticket hypothesis: Finding sparse, trainable neural networks. *International Conference on Learning Representations*, URL <https://openreview.net/forum?id=rJl-b3RcF7>.
- Gagne, D. J., A. McGovern, S. E. Haupt, R. A. Sobash, J. K. Williams, and M. Xue, 2017: Storm-based probabilistic hail forecasting with machine learning applied to convection-allowing ensembles. *Weather and Forecasting*, **32** (5), 1819–1840, <https://doi.org/https://doi.org/10.1175/WAF-D-17-0010.1>.
- Geng, Y.-a., and Coauthors, 2021: A deep learning framework for lightning forecasting with multi-source spatiotemporal data. *Quarterly Journal of the Royal Meteorological Society*, **147** (741), 4048–4062, <https://doi.org/https://doi.org/10.1002/qj.4167>, <https://rmets.onlinelibrary.wiley.com/doi/pdf/10.1002/qj.4167>.
- Gerz, T., C. Forster, and A. Tafferner, 2012: *Mitigating the Impact of Adverse Weather on Aviation*, 645–659. Springer Berlin Heidelberg, Berlin, Heidelberg, [https://doi.org/10.1007/978-3-642-30183-4\\_39](https://doi.org/10.1007/978-3-642-30183-4_39), URL [https://doi.org/10.1007/978-3-642-30183-4\\_39](https://doi.org/10.1007/978-3-642-30183-4_39).
- Hagen, M., and U. Finke, 1999: Motion characteristics of thunderstorms in southern germany. *Meteorological Applications*, **6** (3), 227–239, <https://doi.org/10.1017/S1350482799001164>.
- Hasanin, T., and T. Khoshgoftaar, 2018: The effects of random undersampling with simulated class imbalance for big data. *2018 IEEE International Conference on Information Reuse and Integration (IRI)*, 70–79, <https://doi.org/10.1109/IRI.2018.00018>.
- Herman, G. R., and R. S. Schumacher, 2018: Money doesn’t grow on trees, but forecasts do: Forecasting extreme precipitation with random forests. *Monthly Weather Review*, **146** (5), 1571–1600, <https://doi.org/https://doi.org/10.1175/MWR-D-17-0250.1>.
- Holle, R. L., 2014: Some aspects of global lightning impacts. *2014 International Conference on Lightning Protection (ICLP)*, 1390–1395, <https://doi.org/10.1109/ICLP.2014.6973348>.
- Jardines, A., H. Eivazi, E. Zea, J. García-Heras, J. Simarro, E. Otero, M. Soler, and R. Vinuesa, 2024: Thunderstorm prediction during pre-tactical air-traffic-flow management using convolutional neural networks. *Expert Systems with Applications*, **241**, 122466, <https://doi.org/https://doi.org/10.1016/j.eswa.2023.122466>.
- Kingma, D. P., and J. Ba, 2014: Adam: A method for stochastic optimization. arXiv, URL <https://arxiv.org/abs/1412.6980>, <https://doi.org/10.48550/ARXIV.1412.6980>.
- Kober, K., G. C. Craig, C. Keil, and A. Dörnbrack, 2012: Blending a probabilistic nowcasting method with a high-resolution numerical weather prediction ensemble for convective precipitation forecasts. *Quarterly Journal of the Royal Meteorological Society*, **138** (664), 755–768, <https://doi.org/https://doi.org/10.1002/qj.939>, <https://rmets.onlinelibrary.wiley.com/doi/pdf/10.1002/qj.939>.
- LeCun, Y., J. Denker, and S. Solla, 1989: Optimal brain damage. *Advances in Neural Information Processing Systems*, D. Touretzky, Ed., Morgan-Kaufmann, Vol. 2, URL [https://proceedings.neurips.cc/paper\\_files/paper/1989/file/6c9882bbac1c7093bd25041881277658-Paper.pdf](https://proceedings.neurips.cc/paper_files/paper/1989/file/6c9882bbac1c7093bd25041881277658-Paper.pdf).
- Leinonen, J., U. Hamann, I. V. Sideris, and U. Germann, 2023: Thunderstorm nowcasting with deep learning: A multi-hazard data fusion model. *Geophysical Research Letters*, **50** (8), e2022GL101626, <https://doi.org/https://doi.org/10.1029/2022GL101626>, <https://agupubs.onlinelibrary.wiley.com/doi/pdf/10.1029/2022GL101626>.
- Li, J., C. Forster, J. Wagner, and T. Gerz, 2021: Cb-fusion–forecasting thunderstorm cells up to 6 hours. *Meteorologische Zeitschrift*, 169–184.

- Li, W., H. Chen, L. Han, and J. Xu, 2022: The interpretation of deep learning for convective storm nowcasting. *IGARSS 2022 - 2022 IEEE International Geoscience and Remote Sensing Symposium*, 7922–7925, <https://doi.org/10.1109/IGARSS46834.2022.9883967>.
- Lin, P.-F., P.-L. Chang, B. J.-D. Jou, J. W. Wilson, and R. D. Roberts, 2012: Objective prediction of warm season afternoon thunderstorms in northern taiwan using a fuzzy logic approach. *Weather and Forecasting*, **27** (5), 1178 – 1197, <https://doi.org/10.1175/WAF-D-11-00105.1>.
- Loken, E. D., A. J. Clark, and C. D. Karstens, 2020: Generating probabilistic next-day severe weather forecasts from convection-allowing ensembles using random forests. *Weather and Forecasting*, **35** (4), 1605 – 1631, <https://doi.org/https://doi.org/10.1175/WAF-D-19-0258.1>.
- Markowski, P., and Y. Richardson, 2011: *Mesoscale meteorology in midlatitudes*. John Wiley & Sons, 42-43 pp.
- Mohammed, R., J. Rawashdeh, and M. Abdullah, 2020: Machine learning with oversampling and undersampling techniques: Overview study and experimental results. *2020 11th International Conference on Information and Communication Systems (ICICS)*, 243–248, <https://doi.org/10.1109/ICICS49469.2020.239556>.
- Murphy, A. H., 1973: A new vector partition of the probability score. *Journal of Applied Meteorology and Climatology*, **12** (4), 595 – 600, [https://doi.org/https://doi.org/10.1175/1520-0450\(1973\)012\(0595:ANVPOT\)2.0.CO;2](https://doi.org/https://doi.org/10.1175/1520-0450(1973)012(0595:ANVPOT)2.0.CO;2).
- Ntelekos, A. A., J. A. Smith, and W. F. Krajewski, 2007: Climatological analyses of thunderstorms and flash floods in the baltimore metropolitan region. *Journal of Hydrometeorology*, **8** (1), 88 – 101, <https://doi.org/10.1175/JHM558.1>.
- Palmer, T., 2017: The primacy of doubt: Evolution of numerical weather prediction from determinism to probability. *Journal of Advances in Modeling Earth Systems*, **9** (2), 730–734, <https://doi.org/https://doi.org/10.1002/2017MS000999>, <https://agupubs.onlinelibrary.wiley.com/doi/pdf/10.1002/2017MS000999>.
- Piper, D., M. Kunz, F. Ehmele, S. Mohr, B. Mühr, A. Kron, and J. Daniell, 2016: Exceptional sequence of severe thunderstorms and related flash floods in may and june 2016 in germany – part 1: Meteorological background. *Natural Hazards and Earth System Sciences*, **16** (12), 2835–2850, <https://doi.org/10.5194/nhess-16-2835-2016>.
- Rädler, A. T., P. H. Groenemeijer, E. Faust, R. Sausen, and T. Púčík, 2019: Frequency of severe thunderstorms across europe expected to increase in the 21st century due to rising instability. *npj Climate and Atmospheric Science*, **2** (1), 30.
- Ravuri, S., and Coauthors, 2021: Skilful precipitation nowcasting using deep generative models of radar. *Nature*, **597** (7878), 672–677.
- Reinert, D., and Coauthors, 2020: Dwd database reference for the global and regional icon and icon-eps forecasting system. *Technical report Version 2.1. 8*, Deutscher Wetterdienst.
- Roberts, N. M., and H. W. Lean, 2008: Scale-selective verification of rainfall accumulations from high-resolution forecasts of convective events. *Monthly Weather Review*, **136** (1), 78 – 97, <https://doi.org/10.1175/2007MWR2123.1>.
- Saito, T., and M. Rehmsmeier, 2015: The precision-recall plot is more informative than the roc plot when evaluating binary classifiers on imbalanced datasets. *PLOS ONE*, **10** (3), 1–21, <https://doi.org/10.1371/journal.pone.0118432>.
- Simon, T., P. Fabsic, G. J. Mayr, N. Umlauf, and A. Zeileis, 2018: Probabilistic forecasting of thunderstorms in the eastern alps. *Monthly Weather Review*, **146** (9), 2999 – 3009, <https://doi.org/10.1175/MWR-D-17-0366.1>.
- Simonyan, K., A. Vedaldi, and A. Zisserman, 2014: Deep inside convolutional networks: Visualising image classification models and saliency maps. *Workshop at International Conference on Learning Representations*.
- Sobash, R. A., J. S. Kain, D. R. Bright, A. R. Dean, M. C. Coniglio, and S. J. Weiss, 2011: Probabilistic forecast guidance for severe thunderstorms based on the identification of extreme phenomena in convection-allowing model forecasts. *Weather and Forecasting*, **26** (5), 714 – 728, <https://doi.org/10.1175/WAF-D-10-05046.1>.
- Sobash, R. A., G. S. Romine, and C. S. Schwartz, 2020: A comparison of neural-network and surrogate-severe probabilistic convective hazard guidance derived from a convection-allowing model. *Weather and Forecasting*, **35** (5), 1981 – 2000, <https://doi.org/https://doi.org/10.1175/WAF-D-20-0036.1>.
- Taszarek, M., J. T. Allen, M. Marchio, and H. E. Brooks, 2021: Global climatology and trends in convective environments from era5 and rawinsonde data. *NPJ climate and atmospheric science*, **4** (1), 35.
- Ukkonen, P., and A. Mäkelä, 2019: Evaluation of machine learning classifiers for predicting deep convection. *Journal of Advances in Modeling Earth Systems*, **11** (6), 1784–1802, <https://doi.org/https://doi.org/10.1029/2018MS001561>, <https://agupubs.onlinelibrary.wiley.com/doi/pdf/10.1029/2018MS001561>.
- Vahid Yousefnia, K., T. Böhle, I. Zöbisch, and T. Gerz, 2024: A machine-learning approach to thunderstorm forecasting through post-processing of simulation data. *Quarterly Journal of the Royal Meteorological Society*, **150** (763), 3495–3510, <https://doi.org/https://doi.org/10.1002/qj.4777>.
- Warder, S. C., K. J. Horsburgh, and M. D. Piggott, 2021: Adjoint-based sensitivity analysis for a numerical storm surge model. *Ocean Modelling*, **160**, 101766, <https://doi.org/https://doi.org/10.1016/j.ocemod.2021.101766>.
- Wilks, D. S., 2011: *Statistical methods in the atmospheric sciences*. 3rd ed., International geophysics series, Elsevier Acad. Press, Amsterdam ; Heidelberg [u.a.], XIX, 676 S. pp.
- World Meteorological Organization, 1957: Definition of the tropopause. *Bulletin of the World Meteorological Organization*, **6**, 136–137.
- Yano, J.-I., and Coauthors, 2018: Scientific challenges of convective-scale numerical weather prediction. *Bulletin of the American Meteorological Society*, **99** (4), 699 – 710, <https://doi.org/https://doi.org/10.1175/BAMS-D-17-0125.1>.
- Zhou, K., J. Sun, Y. Zheng, and Y. Zhang, 2022: Quantitative precipitation forecast experiment based on basic nwp variables using deep learning. *Advances in Atmospheric Sciences*, **39** (9), 1472–1486.
- Zängl, G., D. Reinert, P. Rípodas, and M. Baldauf, 2015: The icon (icosahedral non-hydrostatic) modelling framework of dvd and mpi-m: Description of the non-hydrostatic dynamical core. *Quarterly Journal of the Royal Meteorological Society*, **141** (687), 563–579, <https://doi.org/https://doi.org/10.1002/qj.2378>, <https://rmets.onlinelibrary.wiley.com/doi/pdf/10.1002/qj.2378>.